EROSION BEHAVIOR ON A LARGE-SIZED CENTRIFUGAL FAN

N. Aldi[1,a] - N. Casari[1,b] - M. Pinelli[1,c] - A. Suman[1,d] - A. Vulpio[1,e] - P. Saccenti[2,f] - R. Beretta[2,g] - A. Fortini[1,h] - M. Merlin[1,i]

[1] Department of Engineering (DE), University of Ferrara, Ferrara, Italy
[2] Boldrocchi S.r.l., Biassono, Monza e Brianza, Italy

[a] nicola.aldi@unife.it, [b] nicola.casari@unife.it, [c] michele.pinelli@unife.it,
[d] alessio.suman@unife.it, [e] alessandro.vulpio@unife.it, [f] Saccenti@boldrocchi.eu,
[g] beretta@boldrocchi.eu, [h] annalisa.fortini@unife.it, [i] mattia.merlin@unife.it

ABSTRACT

Several production processes involve the use of turbomachinery for the transport of gases with high concentrations of solid particles. Centrifugal fans employed in clinker production operate under severe erosive conditions. To limit the erosive wear of specific fan zones, wear-resistant plates are used. This paper presents a numerical investigation of the erosion behavior of a large-sized centrifugal fan operating in a cement factory. A contaminant characterization is carried out to define particle shape, size distribution and physical characteristics (i.e. density) on which the particle model is based. In addition, the surface analysis and microstructural characterization of the weld-deposited hardfacing alloy provide the wear-resistant coating features. Particles are tracked with a Lagrangian approach on the instantaneous flow fields corresponding to different relative impeller-to-volute positions. The particle impact angle is found to have a significant influence on the erosion of fan surfaces. CFD predictions are in close agreement with on-field erosion detections.

KEYWORDS
centrifugal fan, erosion, computational fluid dynamics, microstructure characterization

NOMENCLATURE

C	coefficient	α	impact angle
d	diameter	γ	inclination angle
E	erosion rate	$\Delta\gamma$	standard deviation of γ
$\mathbf{F}$	force vector	ΔH_r	standard deviation of H_r
$\mathbf{g}$	gravity acceleration vector	μ	dynamic viscosity
H_r	average roughness height	ρ	density
k_s	equivalent sand-grain roughness		
L_r	average roughness length	D	drag
n	velocity exponent	h	hydraulic
R_a	arithmetic average roughness height	i	impact
Re	Reynolds number	L	lift
St	Stokes number	p	particle
t	time	0	reference value
U	averaged velocity		
$\mathbf{u}$	velocity vector	EDS	Energy Dispersive Spectrometer
v	velocity	SEM	Scanning Electron Microscopy
y^+	non-dimensional distance		

INTRODUCTION

The haulage of gases with high concentrations of particles is needed in several production processes. The production of clinker, the base material of the Portland cement, is a typical example of a process where the calcination at a high temperature of the raw material, pulverized by mills and crushers, is delivered by centrifugal fans placed in the most critical points of the plant. The main

objective of these fans is not only the conveying of the material, but also the draft and feed of flue gases and combustion air necessary for the functioning of the main equipment. Since gas velocities inside such process fans can reach very high values, the dragged particles possess a very high kinetic energy that contributes to a material removal from the parts where impacts take place. The erosion damages in stationary parts are mainly related to the efficiency and reliability of the equipment, while the ones on rotating parts are also related to the safety.

The importance of centrifugal fans in cement plants was stressed by McKervey and Perry (1993), according to which the most beneficial improvements to kiln systems can be made by modifications or replacements of fans. In this work, some case histories of fan erosion problems during operation are also reported. Despite the spread of fan erosion issues in industrial plants and the interest of the industrial fan community in minimizing erosion rates through a fan geometry optimization, few studies that deal with centrifugal fan erosion can be found in the open literature. Menguturk and Sverdrup (1985) performed computer calculations of fly-ash particle trajectories and resulting erosion rates for four different types of power plant centrifugal fans to establish their relative erosion tolerance. The authors demonstrated that airfoil centrifugal fans have the highest fly-ash erosion tolerance, although their sensitivity to fan unbalance due to partial filling of blades with ash restricts their use for duty in erosive situations. With regard to this specific aspect, the analysis suggested that the use of single-thickness, backward-curved blading in a wide airfoil fan wheel would overcome the sensitivity of this fan type to unbalance problems, with a small efficiency penalty. Unsteady numerical simulations were also employed by Cardillo et al. (2014) to investigate impeller erosion in a large centrifugal fan (impeller outlet diameter of 3.440 m) installed in a cement production facility. They modeled contaminant (5 μm particles) transport and turbulent dispersion using a Lagrangian approach coupled with a particle cloud tracking model. The study showed non-uniform erosion patterns due to the large unsteadiness and the inherent distortion of the impeller flow as per the impeller-volute interaction. The erosion behavior of large radial fans in recycling plants for end-to-life vehicles was recently analyzed by Fritsche et al. (2017). They explored the respective influence of the spiral volute and blade shape on the erosion rate by means of CFD simulations. It was shown that, for the typical parameters of the investigated fans, the impact angle of metal contaminant (1 mm particles) has a stronger influence than the particle impact velocity. Larger volute designs (i.e. larger spiral pitch angles for volute) were found preferable from an erosion point of view, not because the velocity at their walls is substantially low, but because the particles have steeper angles of incidence and hence cause smaller erosion damage at the walls. Furthermore, it was shown that smaller blade exit angles (i.e. impellers with backward-curved blades) determine fewer erosion rates on the blades as well as on the volute wall.

Fascinating solutions for reducing the erosion issue in centrifugal fans have been investigated taking inspiration from nature. In particular, bionic blade configurations were numerically and experimentally tested in Zhang et al. (2013) and Han et al. (2013), respectively. On the basis of the surface morphology of desert scorpion (Zhang et al., 2013) and tamarisk bark (Han et al., 2013), the authors demonstrated how, by changing the local particle impact angle, the erosion magnitude could be reduced. Even if these solutions appear promising, their implementation on large-sized fans is difficult. The most common approach to limit the erosion in process fans is based on the use of wear-resistant plates, which are placed in correspondence to the fan zones more affected by particle impact. Wear-resistant plates consist of a hardfacing alloy layer weld-deposited on a base plate. The benefits of this solution are reported for example by Mandi and Yaragatti (2012) and, with specific tests, by Holzdeppe (2015).

The erosion rate of the machine components relies on a proper selection of the abrasion-resistant alloys for the deposition of hardfacing layers. Among the commercially available varieties of hardfacing compositions, white cast irons with a high concentration of chromium and carbon are widely used, owing to their low cost-benefit ratio. The remarkable abrasive and erosive wear resistance of such alloys results mainly from the high volume fraction of hard carbides that act as effective barriers to chipping and plowing by erodent particles. As a result, toughness and strain

hardening of the matrix as well as the type, shape, and distribution of hard phases play a key role on the wear-resistance (Chatterjee and Pal, 2003, Sapate and Rama Rao, 2004) and, in turn, on the fan operability.

In this paper, the erosion behavior of a large-sized centrifugal fan installed in a cement plant is studied by means of numerical simulations. At first, the clinker powder is experimentally characterized to determine the particle morphology and the particle size distribution. Topography and microstructural features of the hardfacing alloy weld-deposited on wear-resistant plates used to limit the erosive wear of particular areas within the fan are also established. Particle trajectories are computed with a Lagrangian approach, considering the turbulent dispersion of particles in the fluid phase. In order to take into account the effects of the flow unsteadiness in erosion predictions, a transient simulation is performed and separate particle tracking are carried out on the instantaneous flow fields at three different time instants, corresponding to different relative positions between impeller and volute. In the last section, CFD predictions are compared to on-field erosion detections to validate the numerical models and attain a deeper understanding of the erosion phenomena.

CLINKER POWDER AND WEAR-RESISTANT PLATES CHARACTERIZATION

Previous researches (Sapate and RamaRao, 2000, Sapate and RamaRao, 2006) investigated the influence of erodent particles characteristics on the erosive wear behavior of hardfacing alloys. Sapate and RamaRao (2000) conducted erosive wear tests at different impingement angles and at a velocity of 50 m/s, with, among others, industrial cement clinker erodent. Results indicated that the erosion resistance of hardfacing alloys strongly depends on the relative hardness of erodents. For softer erodents like cement clinker, there is a significant difference in the erosion resistance of hardfacing alloys, which depends only on their hardness. The same authors, in a more recent study (Sapate and RamaRao, 2006), pointed out that the erosion rate of weld hardfacing high chromium cast irons is dependent on the hardness of the erodent particles that, in addition to the impingement angle, influences also the material removal mechanisms. In the light of the above, a preliminary experimental characterization of both the clinker powder and the hardfacing alloy weld-deposited on wear-resistant plates is conducted.

Characterization of Erodent Particles

The morphology of the erodent particles is analyzed by a Zeiss EVO MA 15 Scanning Electron Microscope (SEM). A representative SEM micrograph of the clinker powder is reported in Figure 1a. As can be seen, most of the particles present a rounded shape, with a regular surface morphology. Moreover, in order to evaluate the presence of different-diameter particles within the powder, a quantitative analysis of particle diameter distribution is performed. The particle size distribution is determined by an Optical Particle Sizer 3330 spectrometer and is depicted in Figure 1b, which shows the differential and cumulative particle mass distribution as a function of the particle diameter d_p. The cumulative particle size distribution curve reveals that 80 % of the powder particle mass comprises particles with a diameter less than 5 µm. The overall average density of the powder is determined by an AccuPyc II 1340 pycnometer and it results equal to 2,717 kg/m^3.

Hardfacing Coating Characterization

To prevent the erosive wear of specific areas of the fan, a 5 mm layer of high chromium iron hardfacing alloy is deposited by the flux-cored arc welding method on a 5 mm low-carbon steel base plate. Surface analyses and microstructure characterization of the wear-resistant plate are carried out in order to set up the numerical models. At first, inspection of the areal surface topography of the coating is conducted by a Talysurf CCI-Lite non-contact 3D profilometer.

Figure 2 reports an image of the hardfacing surface, where the side-by-side weld beads as well as the relief checks, due to the stress released by the beads upon cooling of the hard metal, can be identified. Figure 2 shows also the 3D isometric view of the surface from which amplitude parameters are determined in accordance with the standard ISO 4288. In particular, the arithmetic average roughness height R_a is found to be 11.2 μm.

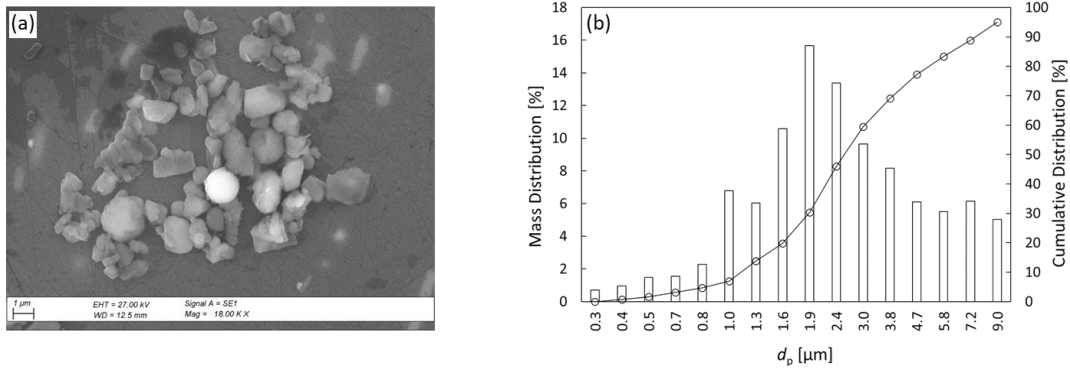On a grounded and polished cross-section of the wear-resistant plate, metallographic

Figure 1: Clinker powder erodent particles: (a) SEM micrograph (18000x) and (b) differential histogram and cumulative particle size distribution curve
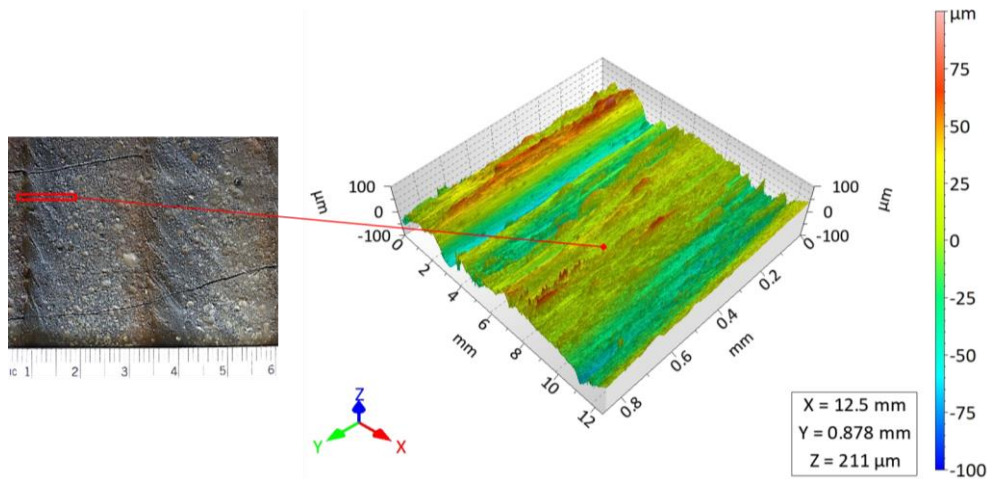

Figure 2: Topography characterizations of the hardfacing: image of the surface including the investigated area and the relative 3D isometric view reconstruction

characterization and hardness measurements are performed. The microstructures of both the hardfacing alloy and the base plate are examined by a Leica DMi8A optical microscope. Microstructural investigations are carried out after chemical etching by Kalling's reagent for the hardfacing alloy and by Nital 2 % for the base plate, respectively. The study of the microstructural features of the alloy is conducted through the aforementioned SEM, equipped with an Oxford X-Max 50 Energy Dispersive Spectrometer (EDS) for semi-quantitative analyses. On the same cross-section, the bulk hardness of the weld hardfacing and of the base plate are determined by a Future-Tech FM-110 Vickers indenter under 1 kg_f load for 15 s dwell time, according to UNI EN ISO 6507-1:2018 standard. Furthermore, the microhardness of the matrix and of the carbides are measured with the same Vickers tester under 100 g_f load for 15 s dwell time.

Microstructural examination of the hardfacing alloy shows that the chromium-rich alloy consists of a large volume fraction of fine niobium-rich MC carbides, randomly dispersed in the austenitic eutectic matrix (907 ± 95 HV0.1), with proeutectic M_7C_3-type chromium carbides. A representative optical micrograph of the hardfacing, including the matrix and carbides labeling, is reported in Figure 3a. Chromium-rich primary carbides are identified on the basis of their morphologies (hexagonal and crystallographically faceted elongated particles in accordance with Liu et al., 2016 and Berns and Fischer, 1987) and confirmed by micro-hardness measurements (1584 ± 119 HV0.1) and by EDS microanalysis (Figure 3b). Regarding the base plate, Figure 3c provides an optical micrograph of the substrate, which reveals the low-carbon steel microstructure consisting of ferritic grains, perlite bands and small flattened sulfide inclusions. Figure 3d shows the hardness profile measured at increasing distances of 1 mm from the top of the weld hardfacing up to the bottom of the base plate. As can be noticed, the bulk hardness is constant along both the hardfacing and base plate thickness, reaching an average hardness of 741 HV1 and 199 HV1, respectively.
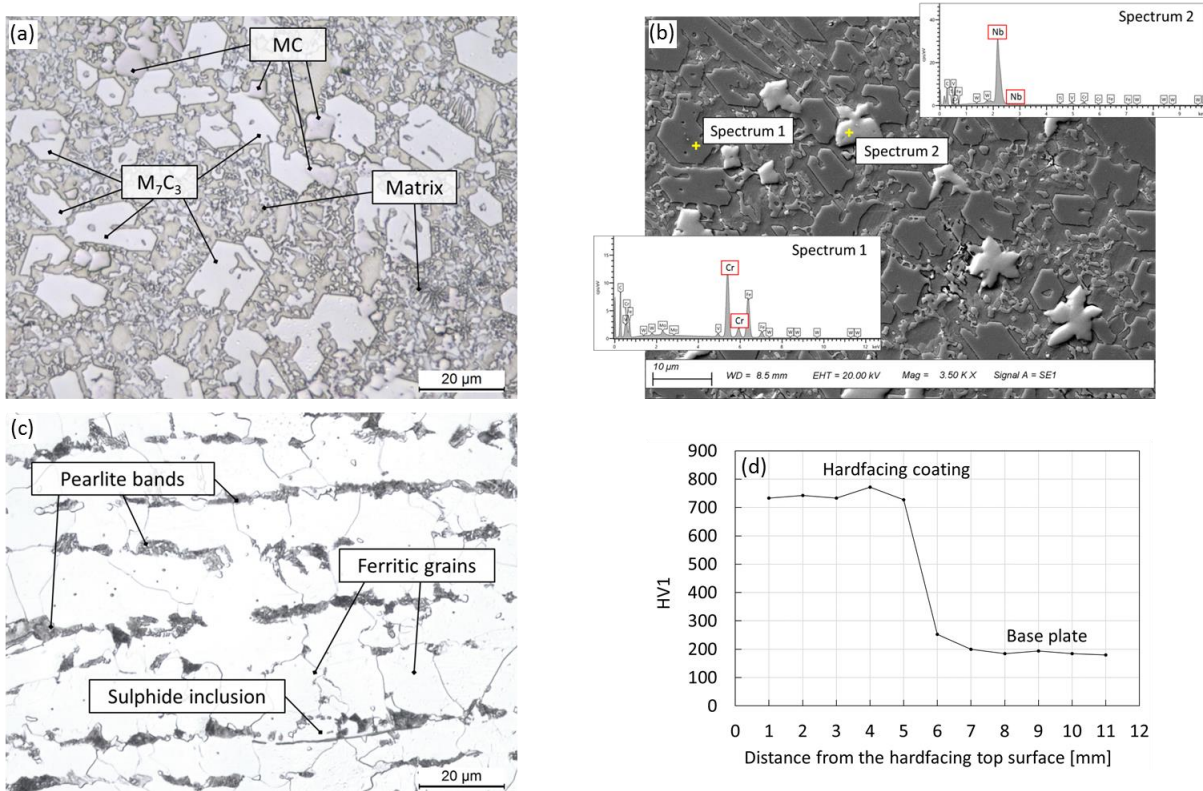
4

Figure 3: (a) Optical and (b) SEM-EDS micrographs of the weld hardfacing alloy. (c) Optical micrograph of the base plate and (d) hardness profile across the wear-resistant plate

FAN NUMERICAL MODEL

The fan under examination is a large-sized single-inlet centrifugal fan operating in a cement plant (Figure 4). It is composed of a constant-width closed impeller, with 12 backward-curved cylindrical blades, and a constant-width spiral volute. The rear side of the impeller disk presents 5 radial ribs for axial thrust balancing. The impeller outside diameter is 4.060 m and fan design rotational speed is 652 rpm. An inlet casing with 3 fixed vanes of constant thickness deflects the flow from the inlet duct, which is arranged normally to the impeller axis, into the axial direction through the fan inlet cone. The inlet cone is bolted to the front side plate of the volute, which is in common with the inlet casing. Wear-resistant plates with a thickness of 10 mm are installed on the pressure side and at the leading edge of fan blades, on the inner surface of the impeller disk, on a portion of the impeller shroud near the blade trailing edge on the pressure side and on a band of the spiral volute facing the impeller outlet section. The locations of wear-resistant plates are highlighted in red in Figure 4.

In order to characterize the internal flow field of the centrifugal fan under study, a time-accurate 3D simulation is performed at the fan operating point. The fan operating point in the cement plant, in terms of mass flow rate and total pressure rise, is 122 kg/s and 8,300 Pa. The simulation is carried
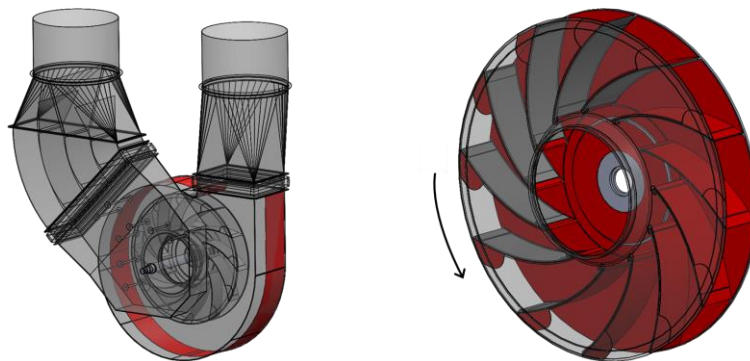

Figure 4: Centrifugal fan and backward-curved impeller (wear-resistant plates in red)

5

out on a computational domain that consists of four fluid domains: two stationary domains (suction domain and volute) and two rotating domains (impeller and impeller sidewall gap domain). A sectional view of the computational domain for the fan is represented in Figure 5. The grid used in the calculation is a hybrid grid with a total number of 57 million elements. The mesh is generated by employing near-wall refinements, with 3 prism layers added on solid walls. The clearance between the impeller and inlet cone is resolved with 8 nodes across the gap span. An enlarged view of the mesh on a blade surface is shown in Figure 5. The first grid points on impeller surfaces (blades, disk and shroud) are positioned in such a way that the y^+ values range from 30 to 300.

The numerical simulation is performed by means of the commercial CFD code ANSYS CFX 16.2. A second-order high-resolution advection scheme is adopted to calculate the advection terms in the flow equations. The turbulence model used in the calculation is the standard k-ε and near-wall effects are modeled with scalable wall functions (ANSYS CFX, 2015). A second-order high-resolution discretization scheme is selected for both turbulent kinetic energy and turbulent dissipation rate equation. In order to account for unsteady rotor/stator interaction effects, transient sliding interfaces are used between rotating and stationary domains. Time marching is controlled through the use of an implicit second-order backward Euler scheme with a physical time step corresponding to 1° impeller rotation. Initial conditions for transient simulation are taken from a steady state solution previously obtained by imposing a frozen rotor model at rotor/stator interfaces. The calculation is carried out for 13 impeller revolutions, at which point the solution is seen to be periodically stable.

An ideal gas approximation is used for kiln exhaust gas handled by the fan. It is also assumed that the fluid has a constant specific heat, dynamic viscosity and thermal conductivity. The relative static pressure, static temperature and flow direction are assigned to the inflow boundary of the inlet duct. The inlet relative static pressure and static temperature are set equal to -7,355 Pa and 118 °C, respectively, and the flow is defined to be normal at the inflow boundary. The operating mass flow rate is imposed at the outflow boundary of the outlet duct. A no-slip boundary condition is applied at the walls, which are also considered as adiabatic. Solid walls are treated as hydraulically smooth with the exception of wear-resistant plates, whose surface roughness is modeled by means of the equivalent sand-grain roughness concept originally introduced by Schlichting (1960). Various empirical correlations have been proposed in literature to relate the equivalent sand-grain roughness k_s to the corresponding arithmetic average roughness height R_a. These correlations were recently reviewed by Bons (2010), who analyzed twenty-three different relations with the ratio k_s/R_a in the range of 2.0 – 6.5. In this paper, the correlation presented by Koch and Smith (1976) is adopted:

$$k_s = 6.2R_a \tag{1}$$

Therefore, the value k_s = 69.4 μm, which corresponds to the experimentally measured average roughness R_a, is imposed on wear-resistant plate surfaces. In order to simulate the presence of
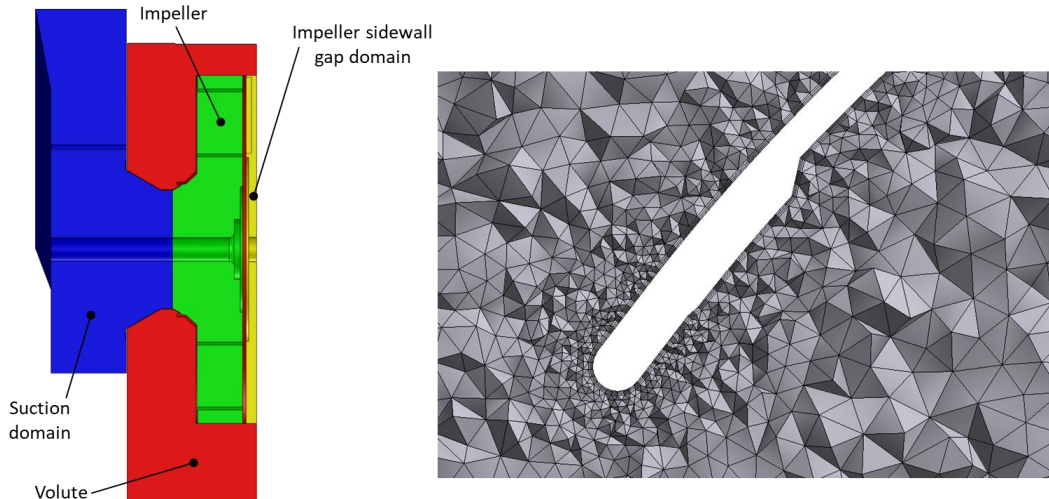

Figure 5: Computational domain for the fan and numerical grid on a blade surface

surface roughness, the near-wall treatment of the k-ε turbulence model is modified with respect to the standard one. More specifically, roughness effects are accounted for by modifying the logarithmic velocity profile (ANSYS CFX, 2015). The distance from the wall of the first grid points on plate surfaces is larger than the imposed k_s value, according to Cadorin et al. (2009).

PARTICLE AND EROSION MODELS

The solution approach for particle trajectory calculation is based on a mathematical model with Eulerian conservation equations for the continuous phase and a Lagrangian frame to simulate a discrete second phase. In this approach, the gas flow field is first simulated and then the trajectories of individual particles are tracked by integrating a force balance equation on the particle. The particle force balance can be written as:

$$\frac{d\mathbf{u}_\mathrm{p}}{dt} = \mathbf{F}_\mathrm{D} + \frac{\rho_\mathrm{p} - \rho}{\rho_\mathrm{p}}\mathbf{g} + \mathbf{F}_\mathrm{L} + \mathbf{F} \tag{2}$$

where the left-hand side represents the inertial force per unit mass acting on the particle and $\mathbf{u}_\mathrm{p}$ is the particle velocity vector. The first and the second term on the right-hand side are the drag force and the buoyancy force per unit particle mass respectively, where ρ_p is the particle density, ρ is the gas density and $\mathbf{g}$ is the gravity acceleration vector. The third term $\mathbf{F}_\mathrm{L}$ refers to the shear-induced lift force per unit mass acting on particles. The last term $\mathbf{F}$ represents additional forces per unit mass on particles, whose significance will be clarified in the following lines of this paragraph.

The general expression for the drag force acting on smooth spherical particles is:

$$\mathbf{F}_\mathrm{D} = \frac{18\mu}{\rho_\mathrm{p} d_\mathrm{p}^2} \frac{C_\mathrm{D} Re_\mathrm{p}}{24}(\mathbf{u} - \mathbf{u}_\mathrm{p}) \tag{3}$$

where μ is the fluid dynamic viscosity, C_D is the drag coefficient, Re_p is the particle Reynolds number:

$$Re_\mathrm{p} = \frac{\rho d_\mathrm{p}|\mathbf{u}_\mathrm{p} - \mathbf{u}|}{\mu} \tag{4}$$

and $\mathbf{u}$ is the fluid velocity vector. The drag coefficient C_D is dependent upon the particle Reynolds number. For spherical particles, three different regimes can be identified:

- at low particle Reynolds numbers ($Re_\mathrm{p} < 0.1$), the drag coefficient is defined by the Stokes' law, $C_\mathrm{D} = 24/Re_\mathrm{p}$ (viscous regime);
- for particle Reynolds numbers that are sufficiently large for inertial effects to dominate viscous effects ($10^3 < Re_\mathrm{p} < 2\cdot10^5$), the drag coefficient becomes independent of the Reynolds number, $C_\mathrm{D} = 0.44$ (inertial regime);
- in the transitional region between the viscous and inertial regimes ($0.1 < Re_\mathrm{p} < 10^3$), both viscous and inertial effects are important and the drag coefficient is thus a function of the particle Reynolds number, which must be determined through experiments. The empirical correlation adopted in the present analysis is due to Schiller and Naumann (1933):

$$C_\mathrm{D} = \frac{24}{Re_\mathrm{p}}\left(1 + 0.15 Re_\mathrm{p}^{0.687}\right) \tag{5}$$

Small particles in a shear flow field experience a lift force $\mathbf{F}_\mathrm{L}$ perpendicular to the direction of relative motion of the two phases. The lift force is most significant in shear layers whose width is comparable to the particle diameter (i.e. boundary layers). The expression for the shear lift force was first obtained by Saffman (1965, 1968) for low Reynolds number flow past a spherical particle. Saffman's expression for the lift force was generalized by Mei and Klausner (1994) to a higher range of particle Reynolds numbers. The Saffman-Mei model (ANSYS CFX, 2015) is applied in this study to calculate the lift force on spherical solid particles.

As stated above, Equation (2) incorporates additional forces $\mathbf{F}$ in the particle force balance that can be important under special circumstances. These additional contributions are: (i) forces that

arise when modeling the flow in a rotating frame of reference (centrifugal and Coriolis forces), (ii) the force required to accelerate the fluid surrounding the particle (virtual mass force) and (iii) the force applied on the particle due to the pressure gradient in the fluid (pressure gradient force). The virtual mass and pressure gradient forces are only significant when the fluid density is comparable to or greater than the particle density. Since the numerical simulations involve the transportation of solid particles in a gaseous flow, the density ratio ρ/ρ_p is much smaller than unity. For this reason, the virtual mass and pressure gradient forces are not considered in the force balance.

The turbulent dispersion of particles in the fluid phase is predicted by using a stochastic tracking model, which includes the effect of instantaneous turbulent velocity fluctuations on the particle trajectories. The instantaneous fluid velocity is decomposed into mean and fluctuating components, the latter governing each particle's turbulent dispersion. The model of turbulent dispersion of particles used in this investigation is due to Gosman and Ioannides (1983). In this model, the fluctuating velocities are assumed to possess a Gaussian probability distribution.

As pointed out by Cardillo et al. (2014), the unsteadiness of the flow may strongly affect the particle transport, impact and erosion behavior. In order to account for the flow unsteadiness in erosion predictions, separate particle injections are performed on the previously-solved gas flow field at different time instants. In particular, the instantaneous flow fields at three different relative positions between impeller and volute are considered for particle trajectory calculation. These relative positions are chosen within a single impeller pitch (equal to 30°), one each 10 degrees rotation, and correspond to the passage of one impeller blade in front of the volute tongue. During the computation of particle trajectories, frozen rotor interfaces are imposed between rotating and stationary domains. At a frozen rotor interface, particles simply cross the interface and continue in the next domain (ANSYS CFX, 2015).

Particles are released at the same local velocities as the gas flow from the inflow boundary of the inlet duct, with equally spaced randomly positioned injection points. In every analysis, the total number of tracked particles is 10^6. This number of particles is selected to satisfy the statistical independence of the results since turbulent dispersion is modeled based on a stochastic approach.

In order to take into account the real composition of the clinker powder which causes the erosion phenomena, the particle density ρ_p is set equal to 2,717 kg/m^3 according to the experimentally measured value. Injected particles are spherical and non-deformable. A particle diameter distribution is specified at the inlet section in accordance with the experimental characterization of the powder previously described. The variation of the Stokes number St, calculated at the inflow boundary of the inlet duct and at the throat section of the inlet cone:

$$St = \frac{\rho_p d_p^2}{18\mu} \frac{U}{d_h} \tag{6}$$

is in the range of $10^{-5} - 8 \cdot 10^{-4}$ and $10^{-4} - 7 \cdot 10^{-3}$, respectively. In Equation (6), U is the averaged fluid velocity at the considered section and d_h is the hydraulic diameter for the cross-section. The total mass flow rate of injected particles is 6.03 kg/s. It is linked to the gas flow rate and the dust load, the latter being equal to 39 g/m^3. Moreover, it is assumed that particles do not affect the fluid flow (one-way coupling) as the particle's volume fraction is very low (<< 10 %).

The change in momentum of particles due to the interaction with solid walls is modeled by imposing coefficients of restitution less than unity at all surfaces. More specifically, for the calculation of particle rebound velocity and direction, the normal and tangential restitution coefficients are set equal to 0.8 and 0.9, respectively. Furthermore, to account for the influence of surface roughness of wear-resistant plates on the particle-wall collision, the Sommerfeld-Frank model (ANSYS CFX, 2015) is adopted. As reported in literature, in fact, both the non-spherical shape of particles (Matsumoto and Saito, 1970a) and wall roughness (Matsumoto and Saito, 1970b) play an important role in determining the bounce behavior of particles. The irregular bouncing model of Frank (2002) is based on the virtual wall model proposed by Sommerfeld (1990). In this model, the bounce of a particle on a rough wall is treated as the bounce on a virtual wall that is inclined with an angle γ with respect to the real wall. The inclination angle γ is a function of surface

roughness and particle diameter. According to Frank (2002), the inclination angle γ is sampled from a Gaussian probability distribution with a mean value of 0° and a standard deviation $\Delta\gamma$:

$$\Delta\gamma = \begin{cases} \arctan\left(2\Delta H_r / L_r\right) & \text{if } d_p \leq L_r / \sin\left[\arctan\left(2H_r / L_r\right)\right] \\ \arctan\left(2H_r / L_r\right) & \text{if } d_p > L_r / \sin\left[\arctan\left(2H_r / L_r\right)\right] \end{cases} \tag{7}$$

where L_r is the average roughness length, H_r is the average roughness height and ΔH_r is the standard deviation of the roughness height. These roughness parameters are directly obtained from the surface roughness measurements carried out on wear-resistant plates.

In the present work, erosion rate on fan internal surfaces is predicted through Finnie's (1960) model of erosive wear as a function of the kinematic characteristics (velocity and angle) of particle impact, the nature and properties of erodent particles and the material properties of the target surface. The implementation of Finnie's model in ANSYS CFX is based on the following expression for the erosion rate E (mass of wall material removed per unit mass of impinging particles):

$$E = \left(v_i / v_0\right)^n f(\alpha) \tag{8}$$

where v_i is the particle impact velocity and $f(\alpha)$ is a function of the particle impact angle α, which is the angle between the impact velocity vector and the surface tangential vector:

$$f(\alpha) = \sin(2\alpha) - 3\sin^2\alpha \quad \text{if } \tan\alpha \leq 1/3 \quad ; \quad f(\alpha) = 1/3\cos^2\alpha \quad \text{if } \tan\alpha > 1/3 \tag{9}$$

The values of the velocity exponent n and the reference velocity v_0 are chosen in accordance with the experimental findings of Sapate and RamaRao (2003). The authors evaluated the effect of erodent particle hardness on velocity exponents of some weld-deposited hardfacing alloys: three steels (named as M1, M2 and M3) and two cast irons (designated as M4 and M5). The erosion tests were conducted with cement clinker (125 µm – 150 µm), blast furnace sinter, silica sand and alumina particles at impingement angles of 30° and 90° and with impact velocities in the range of 50 m/s – 120 m/s. It was found that steady-state erosion rate is dependent on impact velocity by a power law. In the present analysis, the results of erosion tests with cement clinker particles impacting alloys M1 and M5 at an impingement angle of 30° are considered to set up the erosion model. On the basis of these results, n and v_0 are set equal to 1.91 and 8,306 m/s (values for alloy M5), respectively, for wear-resistant plates, while values of 2.10 and 1,706 m/s (values for alloy M1) are fixed on the other fan surfaces.

NUMERICAL RESULTS

Unsteady Flow Field Prediction

The evolution of fan total pressure rise during a complete rotation of the impeller is illustrated in Figure 6. As can be observed, a converged unsteady solution is obtained, which is periodic with the impeller pitch. The overall total pressure rise, determined by averaging the numerical data over one impeller revolution, is 8,021 Pa. The predicted performance parameter differs from the experimentally measured value, equal to 8,301 Pa, of about 3.4 %.

In order to analyze the characteristic features of the unsteady flow field within the fan, Figure 7 reports the velocity field on a 2D section, orthogonal to the axis of rotation and located at 50 % of the blade span, at three different relative positions between impeller and volute. These relative positions correspond to the passage of one impeller blade in front of the volute tongue and refer to the time instants t_1, t_2 and t_3 marked in Figure 6.

The unsteadiness of the flow due to the impeller-volute interaction is clearly visible. Focusing attention on the blade channel that passes in front of the volute tongue between the time instants t_1 and t_3, it is possible to note a progressive distortion of the high-velocity flow at the impeller outlet.

Moreover, the flow conditions inside each blade passage change as the impeller rotates, since the flow experiences a variation in the counter-pressure due to the presence of an asymmetric volute. The blade passage flow exhibits peculiar characteristics depending on the angular position
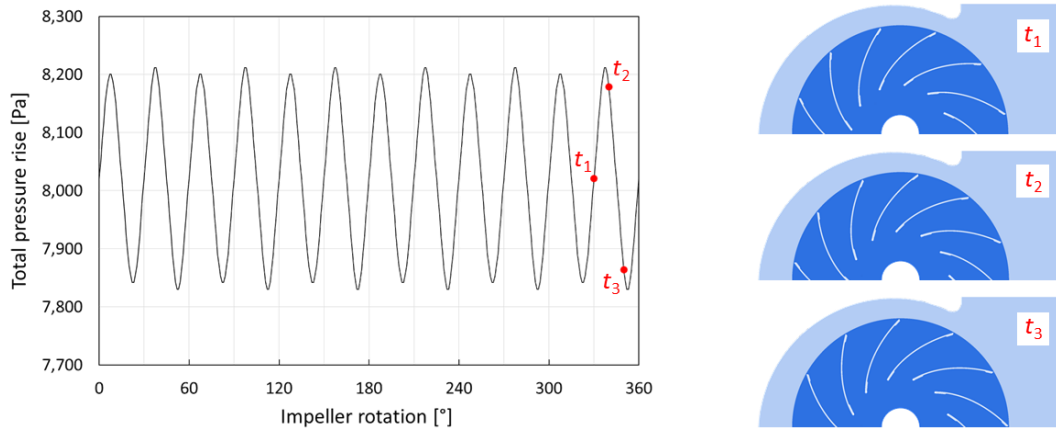
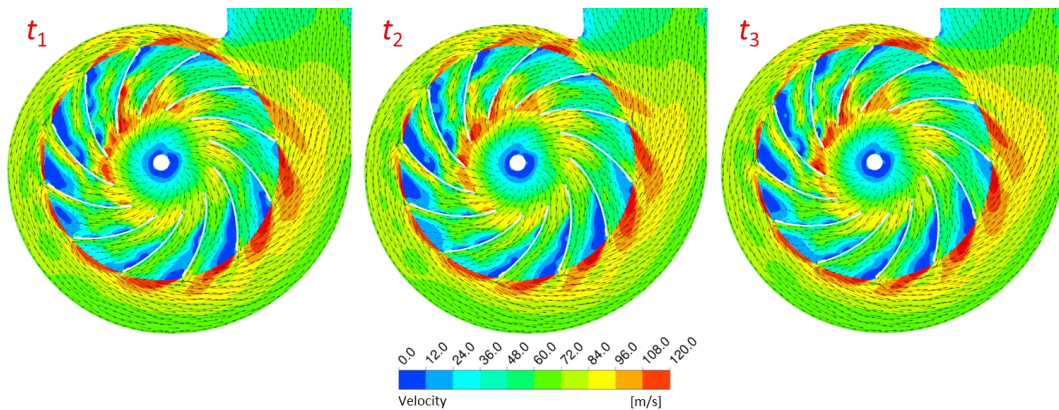**Figure 6: Fan total pressure rise evolution during one impeller rotation**

Figure 7: Velocity field on a 2D section orthogonal to the axis of rotation (50 % of the blade span) at three different relative positions between impeller and volute

of the channel. For the passages in the proximity of the volute tongue, a strong acceleration of the flow can be detected at the leading edge on the blade suction surface, where the local relative velocities reach very high values, up to 120 m/s. For the channels which face the maximum cross-section of the volute, the flow separation on the suction surface, which affects most of the blades, is not present. The described flow features are in agreement with those outlined by Cardillo et al. (2014) for a large-sized centrifugal fan installed in a cement production facility. As stated in the above paragraph, to take into account the effects of the flow unsteadiness in erosion predictions, separate particle tracking are performed on the instantaneous flow fields corresponding to the three time instants t_1, t_2 and t_3 previously identified.

Erosion Analysis

The first analysis deals with the influence of flow unsteadiness on the erosion behavior of the fan. The erosion rate density contour on volute surfaces is depicted in Figure 8 for the considered time instants t_1, t_2 and t_3. It can be seen that the predicted erosion zones and patterns are the same among the three instants. In particular, the effect of the erosion model set up for wear-resistant plates, in terms of the velocity exponent n and the reference velocity v_0, is evident within the volute. Erosion is negligible on a band of the spiral volute facing the impeller outlet section with respect to the other surfaces. This is due to the imposed values of n and v_0, which simulate the presence of wear-resistant plates. Nevertheless, a time variation of the erosion rate magnitude can be observed, that is due to the unsteadiness of the flow caused by impeller-volute interaction. Different flow conditions, in fact, result in different particle impact characteristics, leading to a modification of the erosion intensity.

The effect of the kinematic characteristics of particle impact in erosion predictions is clarified in Figure 9, which refers to the internal surface of the inlet cone. In addition to the erosion rate density contour, the particle impact velocity and impact angle are reported by means of colored particle
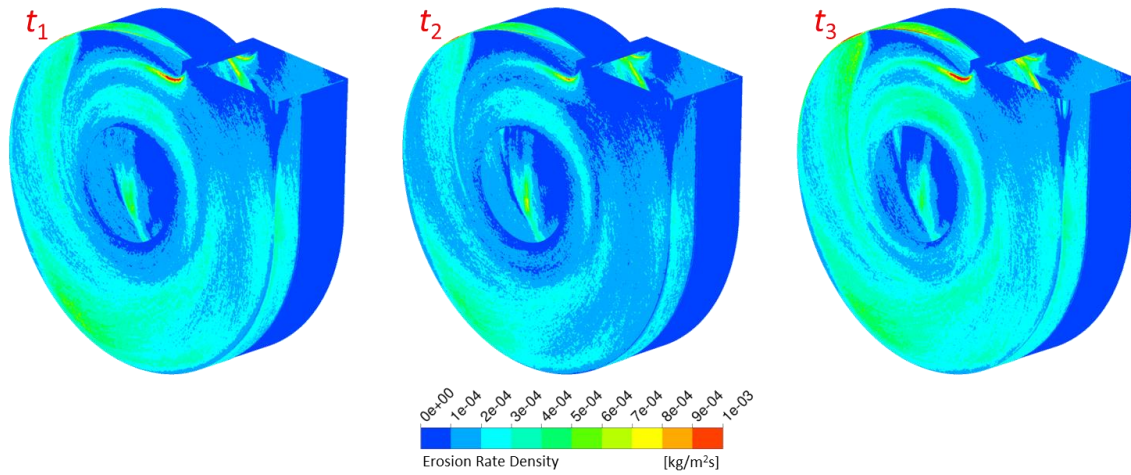
Figure 8: Erosion rate density on volute surfaces at three different time instants

plots. Each dot, which represents a single particle that hits the inlet cone surface, is colored by the impact velocity/angle and is superimposed with respect to the mesh node that provides the surface shape. As can be noticed, both the aforementioned impact parameters contribute in determining the erosion distribution. According to the adopted Finnie's model (Equation (8)), the erosion rate E depends on impact angle α through the function $f(\alpha)$. This function, which is null for $\alpha = 0°$, increases steeply with increasing impact angle, reaching its maximum value for $\alpha \approx 17°$. For higher values of α, the function $f(\alpha)$ decreases, becoming null for $\alpha = 90°$. For this reason, some areas of the inlet cone, where particles impact on the surface at high values of α, are not affected by erosion despite being characterized by very high impact velocities (up to 120 m/s). This strong influence of the impact angle on the erosion of fan surfaces is confirmed by the study of Fritsche et al. (2017).

Finally, a comparison between CFD predictions and on-field erosion detections is presented in order to validate the numerical models. The left image in Figure 10 shows the erosion damage caused by the clinker powder on the volute sidewall, in correspondence to the tongue. This surface is not protected through the use of wear-resistant plates. It is possible to note a significant reduction in wall thickness due to the severe erosive conditions under which the fan operated. As can be observed, the peculiar erosion pattern which characterizes the considered zone is properly reproduced by the model, confirming the reliability of the CFD results.

CONCLUSIONS

This work presents a numerical investigation of the erosion behavior of a large-sized centrifugal fan operating in a cement plant. The numerical simulations are carried out by means of a commercial CFD code. The clinker powder responsible for fan erosion problems is experimentally
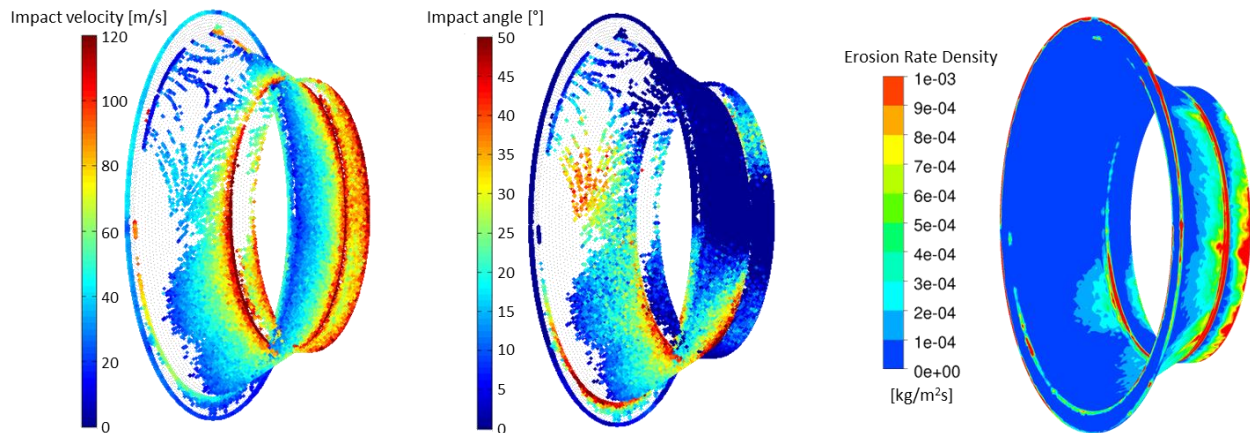

Figure 9: Particle impact velocity, impact angle and erosion rate density on the inlet cone internal surface
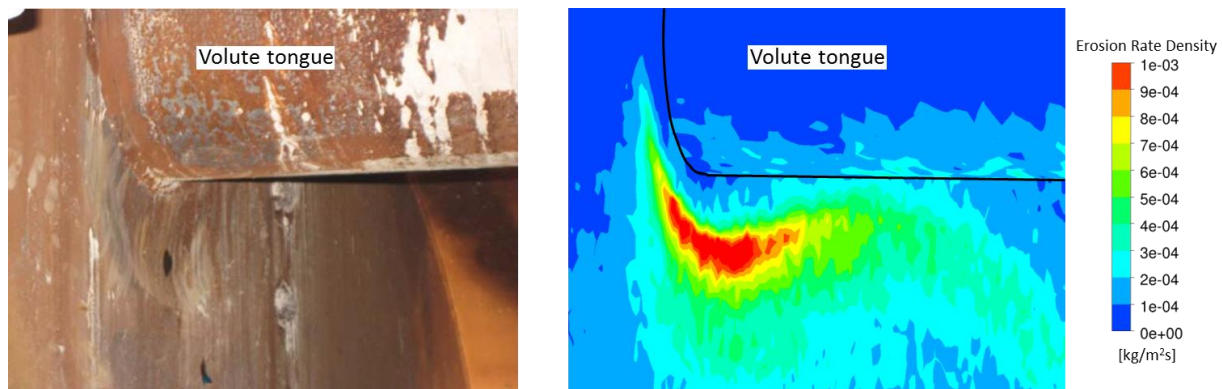
11

Figure 10: Qualitative comparison between actual erosion patterns in correspondence to volute tongue and numerical predictions

characterized to define particle morphology, diameter distribution and physical characteristics of the contaminant. Topography and microstructural features of the hardfacing alloy weld-deposited on wear-resistant plates used to limit the erosive wear of specific fan areas are also established. The gathered data are employed to set up the numerical models. Particle trajectories are computed with a Lagrangian tracking method, accounting for the effects of particle turbulent dispersion in the gas phase. In order to consider the influence of flow unsteadiness in erosion predictions, a transient calculation is performed and separate particle tracking are carried out on the instantaneous flow fields at three different time instants, corresponding to different relative impeller-to-volute positions. The unsteadiness of the flow caused by impeller-volute interaction is found to determine a time variation of the erosion rate magnitude on volute surfaces. This phenomenon is due to a modification of the flow conditions, resulting in different impact characteristics of particles. The effect of the erosion model set up for wear-resistant plates is highlighted by numerical results, since erosion is negligible on the volute surfaces which simulate the presence of the plates. In accordance with the adopted erosion model, the particle impact angle seems to have a significant influence on the erosion of fan surfaces, confirming the findings of other analyses reported in literature. The comparison between CFD predictions and on-field erosion detections demonstrates the reliability of the numerical results and the ability of the model to reproduce the actual erosion patterns.

REFERENCES

McKervey, G. W., Perry, B., (1993), *Fan Applications in the Cement Industry*, Record of Conference Papers 35th IEEE Cement Industry Technical, Toronto, Canada

Menguturk, M., Sverdrup, E. F., (1985), *Computer Calculation of Fan Erosion in Coal-Fired Power Plants. Part 1: Centrifugal Fans*, Int J Turbo Jet Eng, **2**(2), pp. 169–176

Cardillo, L., Corsini, A., Delibra, G., Rispoli, F., Sheard, A. G., Venturini, P., (2014), *Simulation of Particle-Laden Flows in a Large Centrifugal Fan for Erosion Prediction*, Proceedings of ASME Turbo Expo 2014: Turbine Technical Conference and Exposition, Düsseldorf, Germany

Fritsche, M., Epple, P., Steber, M., Rußwurm, H. J., (2017), *Erosion Optimized Radial Fan Impellers and Volutes for Particle Flows*, Proceedings of the ASME 2017 International Mechanical Engineering Congress and Exposition, Tampa, Florida, USA

Zhang, J., Han, Z., Yin, W., Wang, H., Ge, C., Jiang, J., (2013), *Numerical Experiment of the Solid Particle Erosion of Bionic Configuration Blade of Centrifugal Fan*, Acta Metall Sin-Engl, **26**(1), pp. 16–24

Han, Z., Yin, W., Zhang, J., Jiang, J., Niu, S., Ren, L., (2013), *Erosion-Resistant Surfaces Inspired by Tamarisk*, J Bionic Eng, **10**(4), pp. 479–487

Mandi, R. P., Yaragatti, U. R., (2012), *Energy Efficiency Improvement of Auxiliary Power Equipment in Thermal Power Plant through Operational Optimization*, 2012 IEEE International Conference on Power Electronics, Drives and Energy Systems, Bengaluru, India

Holzdeppe, D., (2015), *Particle Flow Erosion at Ventilator Components. Basic Principles of Erosion and Materials/Coatings Resistant against Particle Flow Erosion*, TLT-Turbo GmbH, Zweibrücken, Germany

Chatterjee, S., Pal, T. K., (2003), *Wear behaviour of hardfacing deposits on cast iron*, Wear, **255**(1–6), pp. 417–425

Sapate, S. G., RamaRao, A. V., (2004), *Effect of carbide volume fraction on erosive wear behaviour of hardfacing cast irons*, Wear, **256**(7–8), pp. 774–786

Sapate, S. G., RamaRao, A. V., Garg, N. K., (2000), *Solid Particle Erosion Studies of Weld Hardfacing Deposits*, Mater Manuf Process, **15**(5), pp. 747–759

Sapate, S. G., RamaRao, A. V., (2006), *Erosive wear behaviour of weld hardfacing high chromium cast irons: effect of erodent particles*, Tribol Int, **39**(3), pp. 206–212

Liu, S., Zhou, Y., Xing, X., Wang, J., Ren, Q., Yang, Q., (2016), *Growth characteristics of primary M_7C_3 carbide in hypereutectic Fe-Cr-C alloy*, Sci Rep, **6**, p. 32941

Berns, H., Fischer, A., (1997), *Microstructure of Fe-Cr-C Hardfacing Alloys with Additions of Nb, Ti and, B*, Mater Charact, **39**(2–5), pp. 499–527

ANSYS CFX, (2015), *User Manual*, ANSYS, Inc., Canonsburg, Pennsylvania, USA

Schlichting, H., (1960), *Boundary Layer Theory*, McGraw-Hill, New York, USA

Bons, J. P., (2010), *A Review of Surface Roughness Effects in Gas Turbines*, J Turbomach, **132**(2), p. 021004

Koch, C. C., Smith, L. H., (1976), *Loss Sources and Magnitudes in Axial-Flow Compressors*, J Eng P, **98**, pp. 411–424

Cadorin, M., Morini, M., Pinelli, M., (2009), *Numerical Analyses of High Reynolds Number Flow of High Pressure Fuel Gas Through Rough Pipes*, Proceedings of ASME Turbo Expo 2009: Power for Land, Sea and Air, Orlando, Florida, USA

Schiller, L., Naumann, A., (1933), *A drag coefficient correlation*, Zeitschrift des Vereines Deutscher Ingenieure, **77**(12), pp. 318–320

Saffman, P. G., (1965), *The lift on a small sphere in a slow shear flow*, J Fluid Mech, **22**(2), pp. 385–400

Saffman, P. G., (1968), *The lift on a small sphere in a slow shear flow–Corrigendum*, J Fluid Mech, **31**(3), p. 624

Mei, R., Klausner, J. F., (1994), *Shear lift force on spherical bubbles*, Int J Heat Fluid Fl, **15**(1), pp. 62–65

Gosman, A. D., Ioannides, E., (1983), *Aspects of Computer Simulation of Liquid-Fueled Combustors*, J Energy, **7**(6), pp. 482–490

Matsumoto, S., Saito, S., (1970a), *On the Mechanism of Suspension of Particles in Horizontal Pneumatic Conveying: Monte Carlo Simulation based on the Irregular Bouncing Model*, J Chem Eng Jpn, **3**(1), pp. 83–92

Matsumoto, S., Saito, S., (1970b), *Monte Carlo Simulation of Horizontal Pneumatic Conveying based on the Rough Wall Model*, J Chem Eng Jpn, **3**(2), pp. 223–230

Frank, T., (2002), *Parallele Algorithmen für die numerische Simulation dreidimensionaler, disperser Mehrphasenströmungen und deren Anwendung in der Verfahrenstechnik*, Shaker Verlag, Aachen, Germany

Sommerfeld, M., (1990), *Numerical Simulation of the Particle Dispersion in Turbulent Flow: the Importance of Particle Lift Forces and Particle/Wall Collision Models*, ASME Symposium on Numerical Methods for Multiphase Flows, Toronto, Canada

Finnie, I., (1960), *Erosion of Surfaces by Solid Particles*, Wear, **3**(2), pp. 87–103

Sapate, S. G., RamaRao, A. V., (2003), *Effect of Erodent Particle Hardness on Velocity Exponent in Erosion of Steels and Cast Irons*, Mater Manuf Process, **18**(5), pp. 783–802